npj | flexible electronics

Article

Published in partnership with Nanjing Tech University

https://doi.org/10.1038/s41528-026-00572-2

Ultra-flexible near-infrared vertical cavity surface emitting laser for skin-compatible photoplethysmography monitoring

Check for updates

Younghan Yook[1,5], Jaebin Jeong[1,5], Sunghyun Moon[2], Minseong Seo[1], Haoyan Rong[1], Sangjun Lee[3], Sangin Kim[1,2], Jun-Gyu Choi[2] ✉, Sungjun Park[1,2] ✉ & Jaejin Lee[1,2,4] ✉

Wearable photoplethysmography (PPG) demands stable, long-term light emitters capable of operating under continuous skin contact. Vertical-cavity surface-emitting lasers (VCSELs) offer narrow spectral linewidths, directional emission, and low power consumption; however, conventional devices incorporating thick distributed Bragg reflector (DBR) stacks exhibit mechanical rigidity and inefficient heat dissipation. Here, we present a 6.6-μm-thick ultrathin VCSEL operating at 930 nm, integrated with a near-infrared organic photodetector (NIR-OPD) on a skin-conformal elastomer substrate. A copper-plated heatsink enabled efficient heat dissipation and optical feedback, achieving lasing with only 18 n-DBR. The device emitted 8.25 mW peak power with a 4.53 nm linewidth, retaining 99.3% output over 12 h with minimal heating (1.3 °C). It preserved 97.8% output after 500 bending cycles (6 mm radius) and caused negligible skin irritation. Co-integration with near-infrared OPD enabled stable PPG signal acquisition with <5% amplitude variation, establishing a robust VCSEL–OPD PPG sensor for next-generation wearable biosignal monitoring.

The integration of optoelectronic devices into wearable platforms has transformed biomedical engineering by enabling continuous and real-time monitoring of physiological signals[1–3]. In particular, the coupling of light emitters and photodetectors enables wearable photoplethysmography (PPG) for non-invasive tracking of vital signs such as blood oxygen saturation, heart rate, and blood pressure[4–7]. While flexible photodetectors have been widely developed, the performance of PPG critically depends on the stability of the light source under mechanical deformation, thermal stress, and prolonged skin contact[8–11]. Because PPG sensing relies on optical penetration into biological tissue, light emission in the near-infrared (NIR) window is especially advantageous for maximizing depth and signal fidelity. Thus, an ideal source must combine narrow NIR emission linewidth, high optical output, mechanical flexibility, and thermal robustness while remaining compatible with skin-conformal integration.

Vertical-cavity surface-emitting lasers (VCSELs) have shown strong potential in wearable PPG sensing[12,13]. In contrast, inorganic and organic light-emitting diodes (LEDs) suffer from optical-path variations and broad spectral emission (>30 nm) that reduce the fidelity of PPG signals, particularly under ultrathin, skin-conformal configurations requiring stable optical coupling during prolonged operation[14–16]. On the other hand, VCSELs provide narrow NIR emission linewidth (<0.1 nm), directional output, and low power consumption, making them attractive for high-resolution, long-term biosignal monitoring[17–19]. Their lasing action is sustained by two distributed Bragg reflector (DBR) stacks that form the vertical cavity, with the n-DBR at the bottom side providing essential mirror reflectivity for optical feedback. In addition, VCSELs are compatible with wafer-level processing, supporting scalable integration into thin-film and lightweight form factors[20–22].

State-of-the-art skin-compatible VCSELs exhibit optical output powers of ~7 mW at total device thicknesses of several tens of micrometers[23,24]. However, they require epitaxial growth on rigid substrates such as GaAs, Ge, or Si[25,26], followed by transfer into elastomers for mechanical flexibility[27,28]. The inherently low thermal conductivity of elastomers impedes efficient heat dissipation, resulting in thermal accumulation during extended operation and necessitating heatsinks to suppress spectral drift and optical power degradation[29,30]. Moreover, achieving reliable skin-mounted NIR PPG monitoring remains constrained by thick n-DBR stacks: more than 25 pairs are often required to ensure >99% reflectivity[31,32], causing severe heat accumulation and elevated junction temperature[30]. This thermal buildup degrades lasing performance and risks skin irritation during prolonged

[1]Department of Intelligence Semiconductor Engineering, Ajou University, Suwon, Republic of Korea. [2]Department of Electrical and Computer Engineering, Ajou University, Suwon, Republic of Korea. [3]Research Institute for Information, Communication, and Electronics, Ajou University, Suwon, Republic of Korea. [4]ASEM Ltd., Seongnam, Republic of Korea. [5]These authors contributed equally: Younghan Yook, Jaebin Jeong. ✉e-mail: jungyuchoi93@ajou.ac.kr; sj0223park@ajou.ac.kr; jaejin@ajou.ac.kr

wear. Reducing n-DBR pairs mitigates heating but sacrifices optical feedback, creating a trade-off between thinness and stability. Overcoming these structural and thermal limitations is crucial to enabling practical, long-term NIR PPG monitoring.

In this study, we introduce an ultrathin 930 nm VCSEL integrated with a near-infrared organic photodetector (NIR-OPD) on a skin-conformal elastomer substrate, enabling long-term, reliable PPG monitoring. Utilizing a double-transfer process, the VCSEL is directly bonded onto the Au back-metal/copper-plated heatsink, which simultaneously functions as a reflective optical mirror and an efficient heat spreader. The VCSEL delivered 8.25 mW peak optical power with a 4.53 nm emission linewidth, retaining 99.3% of its output during 12 h of continuous-wave (CW) operation with minimal surface heating of 1.3 °C. Mechanical durability was confirmed by preserving 97.8% output after 500 bending cycles at a 6 mm radius, while pig skin-contact tests verified negligible irritation. When co-integrated with the OPD, the sensor enabled stable NIR PPG acquisition with less than 5% amplitude variation over 12 h, maintaining high signal fidelity. This work establishes a mechanically compliant, thermally robust, and skin-compatible VCSEL–OPD PPG sensor that overcomes the structural and thermal limitations of conventional VCSELs, advancing next-generation wearable biosignal monitoring.

Results

Structural design and optical performance of the ultrathin VCSELs

The ultrathin p-on-n VCSEL was epitaxially grown on a precisely oriented (001) n-GaAs substrate through a low-pressure metal-organic chemical vapor deposition (LP-MOCVD) (Fig. 1a). The ultrathin VCSEL consists of a heavily p-doped GaAs ohmic layer (0.02 μm), 21 pairs of p-DBRs (3.05 μm), InGaAs/GaAsP-based multiple quantum wells (MQWs, 0.29 μm), 18 pairs of n-DBRs (2.75 μm), and a heavily n-doped GaAs ohmic layer (0.5 μm). The number of n-DBR pairs was strategically lowered to achieve enhanced mechanical flexibility and minimize heat accumulation, whereas the counterpart VCSEL employed 38 pairs of n-DBRs (5.45 μm) (Supplementary Fig. 1). The fabrication process for the ultrathin VCSEL involved a double-transfer technique (Fig. 1b). Based on the as-fabricated rigid VCSEL (~350 μm), which indicates the device retains the GaAs substrate, the p-DBRs and MQWs layers underwent mesa etching to isolate each device. A 10 μm oxide aperture was defined via selective lateral oxidation of AlGaAs, whose practical size and design effectively balanced sufficient optical power and thermal stability while maintaining compact side dimensions[26,33]. The heavily p-doped GaAs ohmic layers evaporated onto the p-DBRs strategically reduced both series resistance and contact loss with the front metal, ensuring electrical stability during CW operation[24,34,35]. The Ti/Pt/Au front-metal-evaporated device was then transferred to a wax-coated sapphire carrier, followed by etching the 350-μm-thick bottom GaAs substrate. A lattice-matched n-InGaP layer interfacing the n-DBRs served as an etch-stop, effectively preventing NH_4OH-based etchant from penetrating into the active and mirror regions during the etching process. A Ni/AuGe/Ni/Au back-metal and a 25-μm-thick copper heatsink were sequentially deposited onto the exposed heavily n-doped GaAs ohmic layer surface. The ultrathin VCSEL array was successfully demonstrated on the heatsink via the double-transfer technique, which minimized visible damage and ensured structural integrity of the device. The array consists of approximately 210 VCSEL chips arranged in a 30 × 7 configuration within a 9 mm × 4.5 mm area, demonstrating no fracture even when bent to a radius of 6 mm (Fig. 1c). A top-view scanning electron microscopy (SEM) image of the VCSEL depicts the emission aperture within the circular ring-shaped electrode and the p-contact pads (Fig. 1d). A cross-sectional SEM image of the VCSEL clearly presents its stacked structure with distinguishable component layers (Fig. 1e).

The light–current–voltage (L–I–V) characteristics of the ultrathin VCSEL were measured under CW operation at 25 °C (Fig. 1f), with device-to-device variations (Supplementary Fig. 2). The measured threshold current (I_{th}) and voltage (V_{th}) of the ultrathin VCSEL were 1.67 mA and 1.84 V, respectively, where the peak optical power was 8.25 mW at 38.2 mA of rollover current ($I_{rollover}$). The metal-assisted design maintained a narrow full-width at half maximum (FWHM) even at reduced DBR numbers (Fig. 1g), confirming strong optical confinement. Under an 8 mA injection current, the FWHM corresponding to the peak wavelength around 927 nm was 4.53 nm. Such narrow spectral bandwidth improves wavelength selectivity, often essential for reliable biosignal acquisition in optically scattering biological tissues[36]. Note that the inset depicts the NIR emission from the top-emitting ultrathin VCSEL driven at 6 mA, observed under an optical microscope as a distinct purple beam confined to the aperture region. So far, conventional VCSELs' architecture has required many n-DBR pairs that often exceeded 25 to ensure the bottom mirror reflectivity beyond ~99% (Fig. 1h)[31,32]. While reducing these n-DBR pairs takes advantage of mechanical flexibility for skin-compatible applications, it lowers the reflectivity of the cavity mirrors and increases mirror coupling losses, thereby compromising the optical feedback needed for stable lasing[37]. Meanwhile, the ultrathin VCSEL directly contacted with a reflective back-metal layer demonstrated competitive optical power output despite considerably reduced n-DBR pairs. Consequently, the ultrathin VCSEL with heatsink architecture promised the replacement of conventional VCSELs by simultaneously achieving high optical output, narrow emission linewidth, and mechanical compliance suitable for skin-compatible optoelectronic applications.

Thermal robustness of the ultrathin VCSEL

Long-term operational stability is also a critical requirement for wearable biosignal sensors, where continuous and reliable light emission must be maintained under practical conditions. In conventional rigid VCSELs (Fig. 2a, left), the intrinsically low thermal conductivity of the alternating DBR layers together with the GaAs substrate forms a severe thermal bottleneck, promoting heat accumulation and elevating the junction temperature during CW driving[30]. This thermal buildup leads to Joule heating, free-carrier absorption, scattering losses, and leakage currents, ultimately degrading power-efficiency and device reliability[30,34]. Reducing the number of n-DBR pairs (Fig. 2a, middle) shortens the vertical heat-conduction path and can mitigate thermal resistance; however, heat accumulation still persists because the GaAs substrate continues to dominate the thermal bottleneck. Moreover, decreasing DBR thickness inevitably lowers mirror reflectivity, causing insufficient optical feedback and diminished output power—as experimentally demonstrated by the pronounced performance degradation in rigid VCSELs with only 18 n-DBR pairs (Supplementary Fig. 3). In contrast, the ultrathin VCSEL (Fig. 2a, right) maintains efficient lasing even with just 18 n-DBR pairs, owing to the Au back-metal and copper heatsink layer that simultaneously functions as a high-reflectivity optical mirror and a thermally conductive heat spreader. This dual role restores vertical optical confinement while enhancing heat dissipation. Rigorous coupled-wave analysis (RCWA) further confirms that the back-metal architecture compensates for the reduced DBR reflectivity, sustaining high optical feedback across decreased DBR pair counts (Supplementary Fig. 4). Even in reduced n-DBR pairs, the ultrathin VCSEL demonstrated the narrower FWHM compared to the rigid counterpart, ensuring stronger cavity confinement. Indeed, the ultrathin VCSELs demonstrated much enhanced thermal robustness (Fig. 2b). A wider ambient temperature range (25–55 °C) was commonly employed in VCSEL reliability evaluations[26,31,36]. As junction self-heating during prolonged CW operation elevates the active-region temperature far above ambient levels, even under mild external conditions. As the temperature increased from 25 to 55 °C, the peak optical power of ultrathin VCSEL degraded with the rate of −0.060 mW/°C (−19.5%) over the temperature range, whereas the counterpart rigid VCSEL (38 pairs of n-DBRs) showed −0.093 mW/°C (−42.1%). Meanwhile, the peak wavelength in the emission spectrum was shifted in both VCSELs upon the current input at 8 mA (Supplementary Fig. 5). These red shifts originate from the temperature-induced increase in refractive index and cavity length of the semiconductor layers, which in turn shift the lasing wavelength as the junction temperature rises[38,39]. In the same temperature range, the thermal

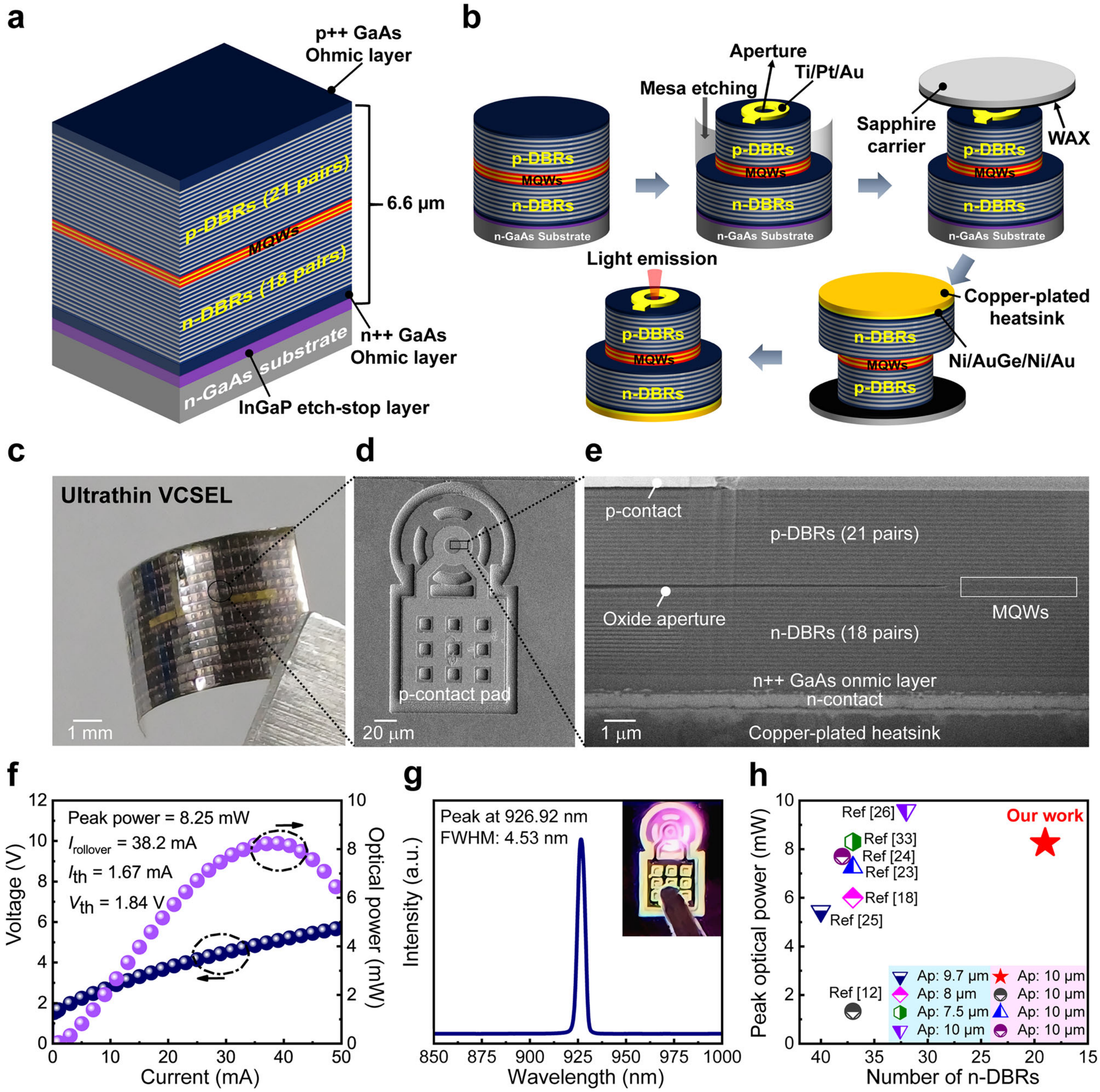

Fig. 1 | Ultrathin near-infrared vertical-cavity surface emitting laser (VCSEL). **a** Epitaxial structure of the ultrathin VCSEL grown on an n-GaAs substrate. **b** Schematic of the double-transfer process for mounting the ultrathin VCSEL onto a copper-plated heatsink. **c** Photograph of the ultrathin VCSEL array on a 25-μm-thick copper-plated heatsink. **d** Top-view and **e** cross-sectional SEM image of the unit VCSEL. **f** *L*–*I*–*V* characteristics of the ultrathin VCSEL under CW operation at 25 °C. **g** Emission spectrum and optical microscope image of the ultrathin VCSEL under lasing. **h** Comparison of peak optical power of reported thin-film and rigid VCSELs as a function of the number of n-DBR pairs.

resistance (R_{th}) for the ultrathin VCSEL was 755 °C/W, representing a 33% reduction compared to 1130 °C/W for the counterpart rigid VCSEL. These results indicate that the proposed device architecture not only mitigates heat accumulation but also ensures spectral stability under elevated thermal stress, attributed to better heat dissipation from the copper-plated heatsink and reduced device thickness[37].

Coupled with thermal reliability, the skin-compatible VCSEL should manage heat accumulation over extended use. The normalized peak optical power over 24 h of CW operation reflected the thermal stability difference between the devices (Fig. 2c). The ultrathin VCSEL exhibited only a ~0.7% reduction in normalized power, whereas the rigid counterpart showed a larger ~5.0% decrease accompanied by a steeper monotonic decline. Furthermore, prolonged operation resulted in an increasing power difference, consistent with the superior thermal management of the ultrathin VCSEL. The surface temperature of the ultrathin and rigid VCSELs were also monitored for extended use (Fig. 2d). In contrast to the rigid VCSEL, which exhibited a rapid and pronounced surface temperature rise ($\Delta T_{surface}$), the ultrathin VCSEL showed a much slower and smaller increase during CW operation. Hourly infrared thermography revealed that the surface temperature of the ultrathin VCSEL rose modestly from 24.2 to 25.5 °C whereas the rigid VCSEL reached a substantially higher temperature of 28.6 °C under identical conditions (Supplementary Fig. 6). Furthermore, the ultrathin VCSELs demonstrated superior thermal safety under prolonged skin contact. Direct skin contact can induce thermally driven irritation, often manifested as visible redness. When operated continuously for 12 h under CW conditions, the pig skin in contact with the rigid VCSEL exhibited

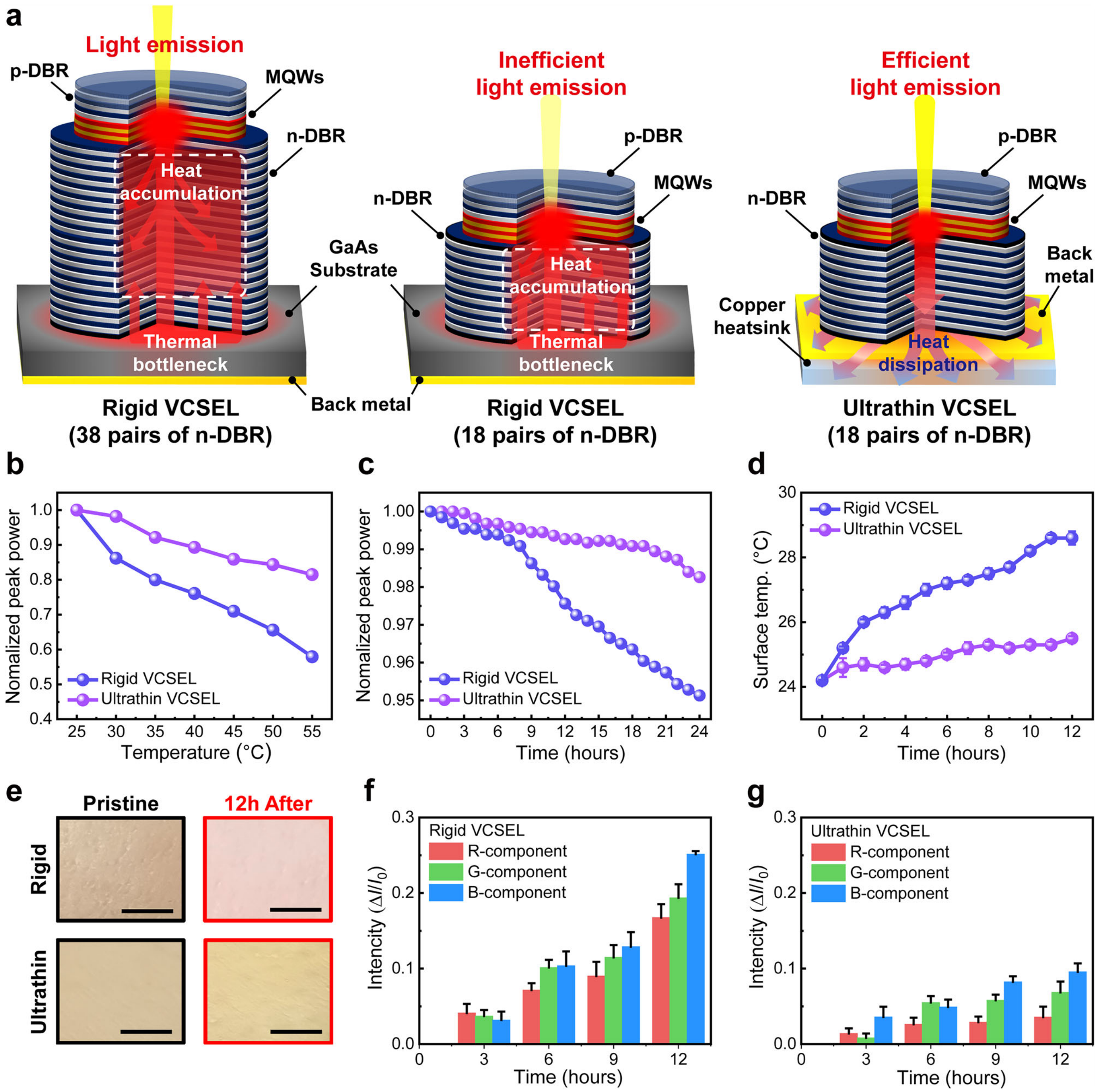

Fig. 2 | Thermal robustness of VCSEL on the skin surface. **a** Schematics of three VCSEL structures showing distinct thermal behaviors during lasing. (Left) A rigid VCSEL with 38 n-DBR pairs experiences severe heat accumulation due to the thick DBR stack and the GaAs thermal bottleneck. (Middle) Reducing the DBR count to 18 shortens the thermal path but still results in heat buildup and degraded light emission due to reduced mirror reflectivity. (Right) The ultrathin VCSEL with 18 n-DBR pairs incorporates a gold back-metal and copper heatsink, enabling efficient heat dissipation and improved optical emission. **b** Normalized peak optical power of rigid (38 pairs of n-DBRs) and ultrathin VCSELs (18 pairs of n-DBRs) under different ambient temperatures, noting thermal robustness evaluation. **c** Normalized peak optical power of both VCSELs measured over 24 h of CW operation at 6 mA, **d** and corresponding surface temperature profiles recorded over 12 h under identical conditions. **e** Photographs of pig skin before and after 12 h of contact with the ultrathin VCSEL (top) and the rigid VCSEL (bottom), comparing the reddening effect during prolonged lasing. Scale bar, 5 mm. Relative RGB intensity change ($\Delta I/I_0$) of pig skin after 12 h of contact with (**f**) rigid VCSEL and **g** ultrathin VCSEL.

localized heating and clear reddening due to insufficient heat dissipation, whereas the skin exposed to the ultrathin VCSEL showed no visible irritation or discoloration (Fig. 2e). More qualitatively, the relative RGB intensity changes ($\Delta I/I_0$) against the contacted periods were monitored (Fig. 2f, g), demonstrating significant difference in each RGB intensity between the rigid and ultrathin VCSELs. Consistent with the visual difference, the red intensity change of the ultrathin VCSEL was 13% higher than that of its counterpart. These findings support the skin compatibility of the ultrathin configuration from a thermal safety perspective and highlight its capability for long-term operation under skin-mounted conditions.

Mechanical robustness of the ultrathin VCSEL

To examine how subtle differences in DBR pair number influence the mechanical flexibility and structural robustness of the devices, we conducted systematic bending and fatigue tests on ultrathin VCSELs incorporating either 18 pairs of n-DBRs (6.6 μm) and 38 pairs of n-DBRs (9.3 μm). Both VCSELs were bent to radii of 13, 11, 8, 6, and 5 mm, with optical power measured at each curvature (Fig. 3a and Supplementary Fig. 7). SEM image of VCSELs subjected to 6-mm bending revealed extensive delamination and surface cracking in the 38-pair device, whereas the 18-pair VCSEL retained its structural integrity without visible defects (Fig. 3b). Reducing the number

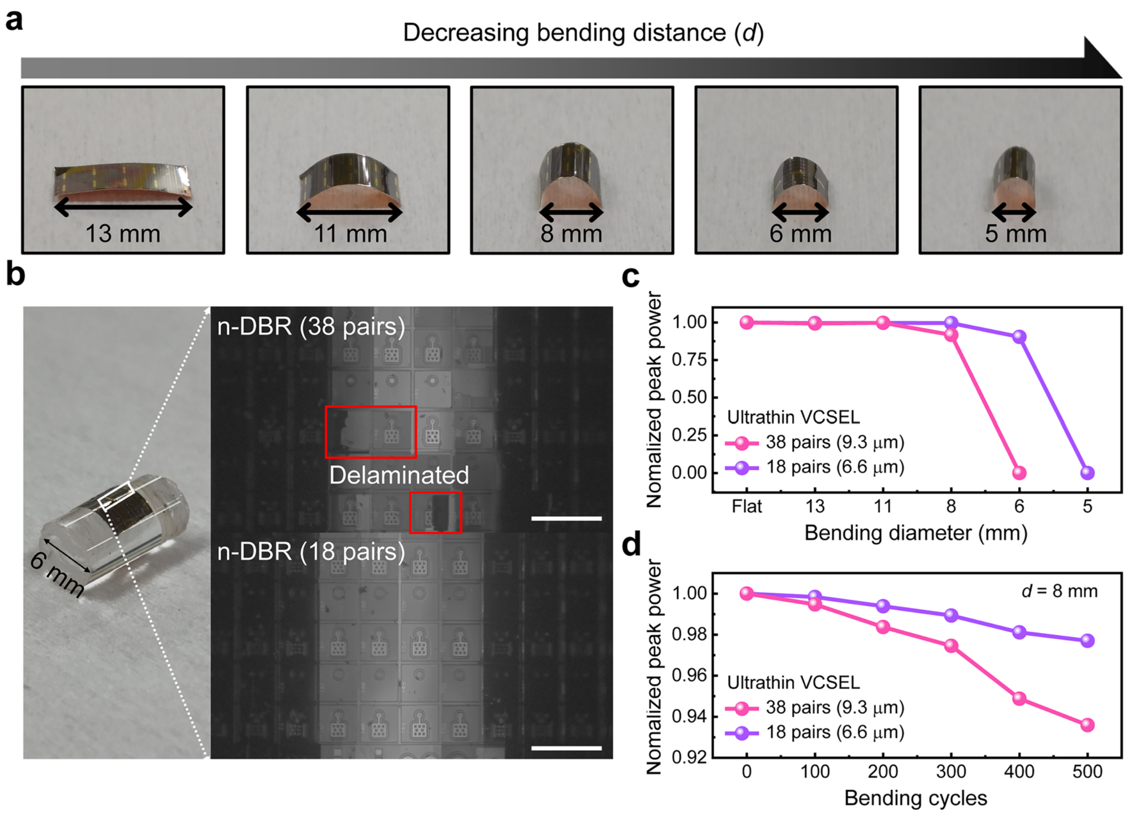

Fig. 3 | Mechanical durability of ultrathin VCSEL. **a** Photographs of ultrathin VCSEL with different bending radii of 13, 11, 8, 6, and 5 mm. **b** Photograph (left) and Optical microscopy images (right) of ultrathin VCSELs with 38 pairs (top) and 18 pairs (bottom) of n-DBRs subjected to deformation under a 6 mm bending radius. Scale bar, 500 μm. **c** Normalized peak optical power of ultrathin VCSELs with 38 pairs and 18 pairs of n-DBR under different bending radii. **d** Normalized peak optical power of ultrathin VCSELs after 500 bending cycles at an 8 mm bending radius.

of n-DBR pairs not only decreases the overall thickness but also lowers the cumulative interfacial strain energy within the multilayer stack. Because additional AlGaAs/AlGaAs DBR pairs amplify elastic-modulus mismatch and thermal-expansion anisotropy, the thinner 18-pair configuration suppresses internal stress buildup during bending and thermal cycling, thereby enhancing mechanical compliance and long-term structural stability. After flattening the bent samples, the 18-pair VCSEL continued to exhibit uniform surface conformity, in contrast to the 38-pair VCSEL, which showed persistent delamination and surface irregularities (Supplementary Fig. 8). In terms of optical performance, the 18-pair VCSEL maintained stable output across bending radii down to 6 mm, showing only a 9.0% decrease in power, whereas deformation below 5 mm led to mechanical failure (Fig. 3c). By comparison, the 38-pair VCSEL showed earlier degradation, with an 8% output drop at 8 mm and full structural breakdown at 6 mm.

Given the cyclic test for extended use, the normalized optical power during 500 repeated bending cycles at 8 mm radius exhibited a significant difference (Fig. 3d). The 18-pair VCSEL exhibited only a 2.2% decrease in output power after 500 cycles, while the 38-pair VCSEL showed a more substantial 6.5% reduction. The higher mechanical rigidity of the 38-pair VCSEL was attributed to its increased bending stiffness resulting from a greater number of n-DBR pairs, which in turn intensified interfacial stress accumulation under repeated deformation[40]. Thicker multilayer structures tend to localize stress during bending, leading to premature crack initiation, accelerated crack propagation, and degradation of electrical performance caused by residual stress. In contrast, the 18-pair VCSEL with reduced n-DBR stacks effectively mitigated stress concentration and mechanical fatigue, preserving both structural and optical integrity even under tight bending and cyclic strain. Consequently, the copper-based back-metal layer played a dual structural role by simultaneously facilitating efficient heat dissipation during continuous operation and mitigating mechanical stress concentration under bending deformation, while further improvements can be achieved through materials variations or multilayer structural optimization of the metallic heat-spreading layer. These findings highlight the potential of the proposed ultrathin VCSEL architecture as a thermally and mechanically robust light source for future skin-conformal wearable biosensing systems.

VCSEL–OPD for PPG signal acquisition

Integration of the optically, thermally, and mechanically robust ultrathin VCSEL with an ultraflexible OPD has illustrated the potential of a highly conformal and fully integrated optoelectronic sensor for wearable PPG sensing. In this work, we employ a single-wavelength VCSEL with a near-infrared-responsive OPD to investigate the fundamental characteristics of PPG signal acquisition using a minimal optoelectronic configuration (Fig. 4a). Mechanical flexibility, lightweight, and ultrathin form factor of OPDs have promised their versatility in skin-conformal applications[41], while featuring low-voltage operation for power-efficiency that serves as a core for sustainable, long-term biosignal monitoring in wearable healthcare systems[10,42]. The OPD, fabricated on a parylene substrate with exceptional mechanical flexibility[43], was positioned at the opposite end of the 330-μm-thick PDMS through a facile delamination process, while the VCSEL was subsequently transferred onto the same PDMS substrate using the surface modification bonding (SMB, see "Methods" section) process[27,28]. The OPD has an inverted layered structure consisting of indium tin oxide (ITO)/zinc oxide (ZnO)/photoactive layer/molybdenum oxide (MoO_3)/Ag (Fig. 4b). The photoactive material, PTB7-Th:IEICO-4F, ensured strong interaction with the ultrathin VCSEL that emitted the peak wavelength ~930 nm, where its bandgap was as narrow as ~1.29 eV[44]. Through a curved configuration, the OPD could successfully record the VCSEL-driven intensity variations altered by pulsatile blood flow changes (Fig. 4c). Despite a vigorous transfer

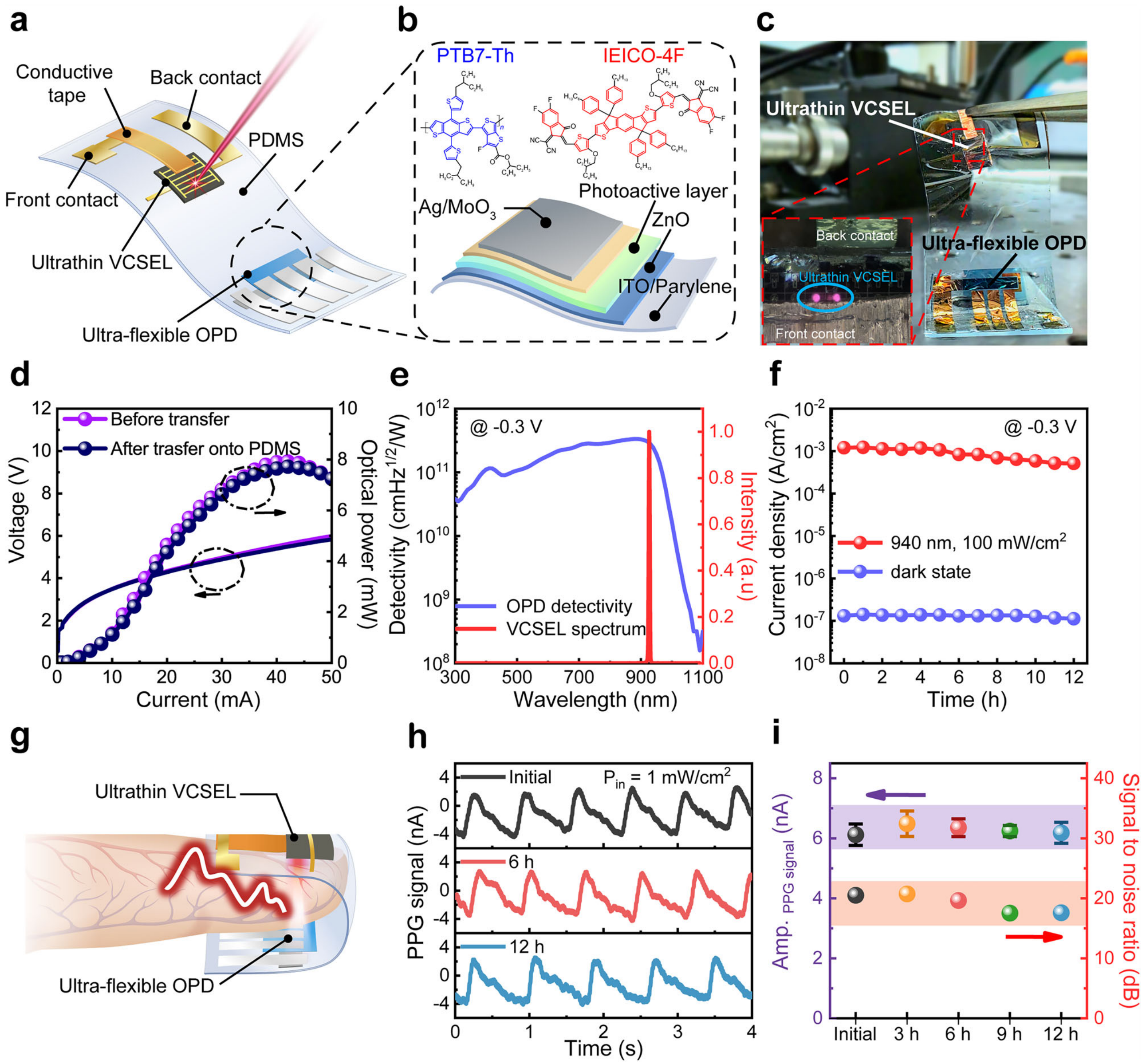

Fig. 4 | Co-integration between ultraflexible near-infrared OPD and ultrathin VCSEL. **a** Schematic of a skin-conformal PPG sensor integrating ultrathin VCSEL and ultraflexible OPD. **b** Schematic of OPD structure with chemical structures of donor (PTB7-Th) and acceptor (IEICO-4F) materials. **c** Photograph of a skin-conformal PPG sensor. **d** $L–I–V$ characteristics of ultrathin VCSEL before and after the transfer process onto the PDMS substrate. **e** Specific detectivity (D^*) of ultraflexible OPD and optical spectrum of ultrathin VCSEL. **f** Current density of the ultraflexible OPD continuously measured over 12 h under 940 nm LED illumination (100 mW/cm^2) and dark conditions at −0.3 V of bias. **g** Schematic of skin-conformal PPG sensor on the fingertip for PPG measurement. **h** PPG signals measured over 12 h using a skin-conformal PPG sensor attached to the fingertip under 1 mW/cm^2 VCSEL illumination. **i** Amplitude and signal-to-noise ratio of the PPG signals during prolonged measurement.

process, the $L–I–V$ characteristics noted consistent electrical performance of the VCSEL before and after transfer onto PDMS substrate (Fig. 4d). Meanwhile, the OPD also demonstrated broad detectivity ranges, of which peak wavelength for specific detectivity of 2.80×10^{11} Jones (~940 nm) was well-matched with those for the VCSEL (Fig. 4e). The OPD exhibited a linear photoresponse (slope = 0.9) over a wide range of incident power under 940 nm LED illumination (Supplementary Fig. 9), indicating stable and sensitive photodetection performance even under low-light conditions. The extended OPD performance over 12 h was also recorded to ensure the compatible long-term PPG monitoring (Fig. 4f), demonstrating stable current levels that ensure its excellent long-term reliability with high sensitivity.

The practical applicability of the integrated device for PPG monitoring was evaluated by mounting it on the fingertip (Fig. 4g). Its ultrathin and lightweight structure ensured intimate skin contact, allowing comfortable wear for 12 h without detachment (Fig. 4h and Supplementary Fig. 10). During this period, the device operated continuously under constant electrical bias, while PPG measurements were obtained at predetermined time points. Clear systolic and diastolic waveforms were captured throughout the 12 h duration, demonstrating stable signal acquisition. Quantitative analysis of the PPG amplitude and signal-to-noise ratio (SNR) at three intervals further verified reliable long-term performance (Fig. 4i). The PPG amplitude throughout the entire period fluctuated only within ~5% (6.49 ± 0.42 nA), and the SNR maintained 86% against the initial value (from 20.5 to 17.6 dB). These results highlight the excellent signal reliability of the integrated sensor under CW operation. Overall, the findings demonstrate that the integrated skin-conformal PPG sensor offers robust performance not only under skin-attached conditions but also under CW operation, making it a promising solution for long-term, high-fidelity physiological signals monitoring applications.

Discussion

We developed a skin-conformal and thermally safe PPG sensor by integrating an ultrathin VCSEL (6.6 µm thick, operating at 930 nm) with an ultraflexible NIR-OPD on a compliant elastomer substrate. The ultrathin VCSEL, fabricated via a double-transfer process incorporating a copper-plated heatsink, effectively mitigated the thermal accumulation and mechanical rigidity of conventional rigid VCSELs, enabling stable, long-term operation under skin-mounted conditions. The device achieved a peak optical power of 8.25 mW with a narrow emission linewidth of 4.53 nm and showed only a 1.3 °C surface temperature rise and 0.7% output loss after 12 h of continuous operation. Pig skin-contact tests revealed negligible visible intensity change, indicating thermal safety and the absence of acute skin irritation. It also maintained >97% optical output after 500 bending cycles at a 6 mm bending radius, confirming excellent mechanical resilience. When co-integrated with the NIR-OPD, the sensor enabled stable PPG acquisition with <5% amplitude variation over 12 h, maintaining high signal fidelity. These findings demonstrate that the ultrathin VCSEL–OPD sensor provides thermally stable, mechanically robust light emission, representing a promising foundation for next-generation skin-integrated wearable healthcare systems. The demonstrated device architecture is also readily extendable to other optical sensing and illumination modalities, and integration of additional functional modules for fully autonomous wearable operation is a logical direction for further development.

Methods

Epitaxial growth

Ultrathin top-emitting VCSELs operating at 930 nm were grown on (001)-oriented n-GaAs substrates using a low-pressure metal-organic chemical vapor deposition (LP-MOCVD) system. The group III precursors used were trimethylgallium (TMGa), trimethylaluminum (TMAl), and trimethylindium (TMIn), while group V sources included arsine (AsH_3) and phosphine (PH_3). For doping, silane (SiH_4) and carbon tetrabromide (CBr_4) were introduced to form highly n-type and p-type GaAs layers, respectively. The epitaxial stack was composed of a 350-µm-thick GaAs substrate, a 100-nm-thick InGaP etch-stop layer for substrate removal selectivity, a heavily doped n-GaAs ohmic layer, 18 pairs of n-type AlGaAs/ AlGaAs distributed Bragg reflectors (DBRs) with a total thickness of 2.75 µm, five periods of InGaAs/GaAsP multiple quantum wells (MQWs) for the active region, 21 pairs of p-type DBRs (3.05 µm total thickness), and a top p-doped GaAs contact layer. To define the emission aperture, a high-aluminum-content $Al_xGa_{1-x}As$ layer was grown above the MQW region. This layer enabled the formation of a 10 µm oxide-confined aperture through selective lateral oxidation in the subsequent fabrication process. The InGaP etch-stop layer played a crucial role in protecting the active and mirror layers from NH_4OH-based etching during substrate removal, ensuring structural integrity.

Thin-film VCSEL fabrication

The fabrication of ultrathin top-emitting VCSELs involved a dual-transfer technique designed to integrate the optoelectronic structure with a 25-µm-thick copper-plated heatsink. Device isolation was first achieved by mesa etching to separate individual VCSELs. A high-Al-content $Al_xGa_{1-x}As$ layer positioned above the MQW region underwent selective lateral oxidation to define a 10 µm oxide-confined aperture for current and optical confinement. Following this, Ti/Pt/Au metal layers were deposited as the front metal on the top GaAs contact layer via electron-beam evaporation. To facilitate substrate removal, the processed wafer was bonded onto a temporary sapphire carrier using adhesive wax, applied under controlled conditions (150 °C for 2 min). The thick GaAs substrate was then etched away using an NH_4OH-based solution, followed by selective removal of the InGaP etch-stop layer with an HCl-based etchant, exposing the underlying n-doped GaAs ohmic layer. For back-side metallization, a Ni/AuGe/Ni/Au multilayer contact was formed on the exposed n-GaAs. Prior to metal plating, the surface was activated using an Ar plasma treatment to improve adhesion between the subsequent copper layer and the underlying metal stack. A bilayer of Cr (30 nm) and Ti (300 nm) was sputtered onto the contact surface to serve as seed layers. Electrochemical deposition was then used to grow a 25-µm-thick copper layer under a current density of 1 ASD for 2.5 h, forming a mechanically robust heatsink directly attached to the n-side of the VCSEL. The final device structure was completed by detaching the temporary carrier, yielding free-standing ultrathin VCSELs directly integrated with copper-plated heatsinks. Throughout the fabrication process, no structural damage or delamination was observed, confirming the reliability of the transfer and bonding steps for high-yield device realization. For scalable manufacturing, established wafer-level approaches such as epitaxial lift-off for substrate reuse, batch deposition of reflective and thermal metal layers, and panel-level transfer techniques can be adopted without altering the core device architecture.

VCSEL characterization

The electrical and optical characteristics of the 930 nm ultrathin VCSELs were evaluated under CW operation. Devices were mounted on a vacuum stage equipped with a rotary pump and an actively controlled temperature platform. A Keithley 2602B source-measure unit (Keithley Instruments Inc.) was used to apply current and measure the *L–I–V* characteristics. Temperature was regulated from −30 °C to 95 °C with a precision of ±0.1 °C using a low-temperature bath system (Tokyo Rikakikai Co., Ltd.). The 930 nm emission from the VCSEL aperture was collected using a silicon photodiode (Hamamatsu, 2201 model). Spectral measurements were performed using a fiber-coupled spectrometer (Ocean Optics Maya 2000 PRO), enabling detailed analysis of wavelength shifts and linewidth variations under different thermal and electrical conditions. A thermal resistance (R_{th}) of the fabricated ultrathin and rigid VCSEL was determined from the temperature rise with dissipated electrical input power, expressed as follows:

$$R_{th} = \Delta T/\Delta P_{diss} = (\Delta\lambda/\Delta P_{diss})/(\Delta\lambda_{peak}/\Delta T) \quad (1)$$

Surface temperature changes of ultrathin and rigid VCSEL were monitored using a thermal imaging camera (Dongguan Bufan Electronics Co., Ltd., A-BF RX-700), and photographs were captured hourly.

Skin-contact thermal safety test

Skin compatibility test was conducted by placing the ultrathin VCSEL and rigid VCSEL in direct contact with pig skin under ambient conditions for 12 h of continuous operation. RGB color intensity variations of the pig skin were quantified using the EclipsePalette software based on the high-resolution images obtained after exposure. The red, green, and blue intensity changes were used as indicators of thermal irritation to evaluate skin compatibility under skin-contact conditions.

Mechanical deformation test

Mechanical bending tests were performed on ultrathin 18-pair VCSELs and 38-pair VCSELs with similar lateral sizes. The devices were manually bent around cylindrical rods with curvature radii of 13 mm, 11 mm, 8 mm, 6 mm, and 5 mm. Optical power output was measured at each bending condition to evaluate mechanical resilience. The emitted 930 nm light from the VCSEL aperture was collected using a silicon photodiode (Hamamatsu, 2201 photodiode), and the normalized optical power was recorded under constant current injection (6 mA) at each radius. For fatigue testing, 500 repeated bending cycles were applied at an 8 mm radius, and optical output was recorded every 100 cycles to assess durability under cyclic mechanical stress.

Ultraflexible OPD fabrication

To fabricate an ultraflexible OPD, glass substrates were sequentially cleaned using ultrasonic treatment in detergent, deionized water, acetone, and isopropyl alcohol, with each step lasting 5 min. To facilitate easy delamination from the glass substrate, a fluorinated polymer blend solution (Novec 1700:7100, 1:10 vol%, 3 M™) was spin-coated onto the glass substrate at 2000 rpm for 1 min. A 1-μm-thick parylene film was deposited onto the fluorinated polymer/glass substrate via chemical vapor deposition and annealed at 120 °C for 1 h. For surface planarization of the parylene film, a 500-nm-thick epoxy layer (SU-8 3005, MicroChem) was spin-coated at 5000 rpm for 1 min, pre-baked at 95 °C for 2.5 min, exposed to UV light for 4 min, and finally annealed at 120 °C for 1 h. A 150-nm-thick ITO was deposited via sputtering without substrate heating, patterned using photolithography, and etched using a wet etching process. A ZnO nanoparticle layer was spin-coated at 2000 rpm for 30 s. The poly(4,8-bis(5-(2-ethylhexyl)thiophen-2-yl)benzo[1,2-b;4,5-b′]dithiophene-2,6-diylalt-(4-(2-ethylhexyl)-3-fluorothieno[3,4-b]thiophene-)-2-carboxylate-2-6-diyl) (PTB7-Th), and 2,2′-((2Z,2′Z)-(((4,4,9,9-tetrakis-(4-hexylphenyl)-4,9-dihydro-sindaceno[1,2-b:5,6-b′]-dithiophene-2,7-diyl)bis(4-((2-ethylhexyl)oxy)thiophene-5,2-diyl))bis(methanylylidene))bis(5,6-difluoro-3-oxo-2,3-dihydro-1H-indene-2,1-diylidene))dimalononitrile (IEICO-4F) blended solution (1:1.5 weight ratio, total concentration: 25 mg/mL in chlorobenzene) was spin-coated at 2000 rpm for 30 s in an argon-filled glove box. Finally, a MoO_3 (5 nm) and Ag (100 nm) were sequentially deposited via thermal evaporation under high vacuum conditions (<2.0×10^{-6} Torr).

Ultraflexible OPD characterization

J–*V* curves were obtained using a source-measure unit (Keithley 2400) under dark conditions and under 940 nm LED illumination (M940F3, THORLABS). The external quantum efficiency (EQE) was measured using a Spectral QE Measurement System (TNE TECH CO., LTD, Korea). The EQE values were obtained as a function of wavelength in the range of 300~1100 nm using a 300 W Xe lamp as the light source, and the calibration was performed using a Si photodiode in the 300–960 nm wavelength range, and an InGaAs photodiode in the 960~1100 nm wavelength range. The spectral noise current was measured by a dynamic signal analyzer (35670A, Alignment) connected to the device through a preamplifier (SR570). The specific detectivity (D^*) based on the noise equivalent power is $D^* = (A\ \Delta f)^{1/2} R/i_{noise}$, where R is the responsivity, A is the effective photodetector area for the devices, Δf is the detection bandwidth, and i_{noise} is the noise current measured under dark state.

Integration of OPD with VCSEL for PPG measurement

The PDMS was prepared by blending the base and the curing agent at a 10:1 weight ratio. The mixture solution was spin-coated onto the glass substrate at 1000 rpm for 10 seconds and subsequently cured at 60 °C for 2 h. A Ti/Pt/Au (35/5/360 nm) electrode was deposited by electron-beam evaporation on the PDMS substrate as the electrical contact. The ultrathin VCSEL was transferred onto the PDMS substrate using the SMB process. For electrical connection, a conductive adhesive tape was applied to bridge the top contact of the ultrathin VCSEL and the Au electrode on PDMS. Separately, the ultraflexible OPD was carefully peeled off from the supporting glass and then laminated onto the PDMS substrate.

Surface modification bonding (SMB) process

The back contact of the ultrathin VCSEL was treated with oxygen plasma (60 W and 50 sccm flow rate condition for 1 min), and then oxygen plasma-activated VCSEL was immersed in a silane solution (100 mL DI water: 1 mL (3-aminopropyl) triethoxysilane (APTES)) for 20 min. Simultaneously, oxygen plasma treatment was performed on the Au electrode of the PDMS substrate under the same conditions. The plasma-activated PDMS substrate was mounted on the silanized back contact of the ultrathin VCSEL, forming a strong bond at room temperature.

Long-term PPG signal sensing

For long-term PPG measurement, the skin-conformal PPG sensor was carefully delaminated from the supporting glass and attached to the fingertip. A source-measure unit (Keithley 2400, Tektronix) was employed to supply bias voltages to the ultrathin VCSEL and OPD. The PPG signal was recorded using an SR570 preamplifier (Stanford Research System) and DAQami at a sampling rate of 1 kHz. Customized MATLAB code was used to calculate the amplitude and SNR of the PPG signal. The SNR was calculated with the following equation:

$$\mathrm{SNR(dB)} = 10\log_{10}\left(\frac{\int_{0.5\,Hz}^{10\,Hz} |I(w)|^2 dw}{\int_{10\,Hz}^{\infty} |I(w)|^2 dw}\right) \tag{2}$$

where $I(\omega)$ is the intensity of the power spectrum at frequency ω. The signal power was the total spectral power in the range of 0.5–10 Hz, while the noise power was the total spectral power in the range of 10 Hz to the maximum frequency[45]. The approval from a national or institutional ethics board/committee was obtained by the Ajou University Institutional Review Board (AjouIRB, 202410-HB-003).

Ethics declarations

The participant in the biosignal sensing experiments was a co-author of this work and provided informed consent.

Data availability

The datasets generated and/or analyzed during the current study are not publicly available due to ongoing supplementary research but are available from the corresponding author on reasonable request.

Code availability

No custom code was used in this study. We provide the code utilized in this study to support public availability, which can be deposited in a public repository of Nature journals.

Received: 15 January 2026; Accepted: 19 March 2026;
Published online: 04 April 2026

References

1. Yun, S. H. & Kwok, S. J. J. Light in diagnosis, therapy and surgery. *Nat. Biomed. Eng.* **1**, 0008 (2017).
2. Humar, M. et al. Toward biomaterial-based implantable photonic devices. *Nanophotonics* **6**, 414–434 (2017).
3. Bansal, A., Yang, F., Xi, T., Zhang, Y. & Ho, J. S. In vivo wireless photonic photodynamic therapy. *Proc. Natl. Acad. Sci. USA* **115**, 1469–1474 (2018).
4. Kong, D., Zhang, K., Tian, J., Yin, L. & Sheng, X. Biocompatible and Biodegradable Light-Emitting Materials and Devices. *Adv. Mater. Technol.* **7**, 2100006 (2022).
5. Nazempour, R., Zhang, Q., Fu, R. & Sheng, X. Biocompatible and implantable optical fibers and waveguides for biomedicine. *Materials* **11**, 1283 (2018).
6. Kim, J. et al. Miniaturized battery-free wireless systems for wearable pulse oximetry. *Adv. Funct. Mater.* **27**, 1604373 (2017).
7. Han, D. et al. Pulse oximetry using organic optoelectronics under ambient light. *Adv. Mater. Technol.* **5**, 1901122 (2020).
8. Nam, M. et al. Highly reliable and stretchable OLEDs based on facile patterning method: toward stretchable organic optoelectronic devices. *npj Flex. Electron.* **8**, 17 (2024).
9. Kang, K. S., Jeong, S. Y., Jeon, Y., Kwon, J. H. & Choi, K. C. Enhancing flexibility and reliability in wearable OLEDs through silbione-blended hybrimer-based encapsulation. *npj Flex. Electron.* **9**, 49 (2025).
10. Choi, D. et al. Vertically stacked all-organic ring-shaped pulse oximetry sensor with ultra-low power consumption and low-luminance operation. *npj Flex. Electron.* **9**, 26 (2025).
11. Zhou, H., Kim, H., Jeong, W. J. & Lee, T. Toward intrinsically stretchable OLEDs with high efficiency. *Adv. Mater.* **37**, 2420008 (2025).

12. Kang, D. et al. Compliant, heterogeneously integrated GaAs micro-VCSELs towards wearable and implantable integrated optoelectronics platforms. *Adv. Opt. Mater.* **2**, 373–381 (2014).
13. Li, C. et al. Wearable and biocompatible blood oxygen sensor based on heterogeneously integrated lasers on a laser-induced graphene electrode. *ACS Appl. Electron. Mater.* **4**, 1583–1591 (2022).
14. Pribadi, E. F., Pandey, R. K. & Chao, P. C.-P. Optimizing a novel PPG sensor patch via optical simulations towards accurate heart rates. *Microsyst. Technol.* **26**, 3409–3420 (2020).
15. Wei, Y. et al. Double-path acquisition of pulse wave transit time and heartbeat using self-mixing interferometry. *Opt. Commun.* **393**, 178–184 (2017).
16. White, M. S. et al. Ultrathin, highly flexible and stretchable PLEDs. *Nat. Photon.* **7**, 811–816 (2013).
17. Moon, S. et al. High-performance thin-film VCSELs integrated with a copper-plated heatsink. *Adv. Mater. Interface* **10**, 2300191 (2023).
18. AL-Omari, A. N., Alias, M. S., Ababneh, A. & Lear, K. L. Improved performance of top-emitting oxide-confined polyimide-planarized 980 nm VCSELs with copper-plated heat sinks. *J. Phys. D: Appl. Phys.* **45**, 505101 (2012).
19. Koyama, F. Recent advances of VCSEL photonics. *J. Lightwave Technol.* **24**, 4502–4513 (2006).
20. Jayaraman, V. et al. High-speed ultra-broad tuning MEMS-VCSELs for imaging and spectroscopy. *Proc. SPIE* **8763**, 87630H (2013).
21. Tsai, T.-H. et al. Ultrahigh speed endoscopic optical coherence tomography for gastroenterology. *Biomed. Opt. Express* **5**, 4387 (2014).
22. Cheng, C.-H. et al. 850/940-nm VCSEL for optical communication and 3D sensing. *Opto-Electron. Adv.* **1**, 18000501–18000511 (2018).
23. Kwon, O. et al. Highly efficient thin-film 930 nm VCSEL on PDMS for biomedical applications. *Sci. Rep.* **13**, 571 (2023).
24. Moon, S. et al. Top-emitting 940-nm thin-film VCSELs transferred onto aluminum heatsinks. *Sci. Rep.* **12**, 565 (2022).
25. Wan, Z. et al. Monolithically integrated 940 nm VCSELs on bulk Ge substrates. *Opt. Express* **32**, 6609 (2024).
26. Wang, C., Li, C. & Wang, Z. Analysis of optical and thermal properties of 940-nm vertical-cavity surface-emitting lasers. *Opt. Quant. Electron* **54**, 438 (2022).
27. Sunkara, V., Park, D.-K. & Cho, Y.-K. Versatile method for bonding hard and soft materials. *RSC Adv.* **2**, 9066–9070 (2012).
28. Nam, Y. et al. Ultra-thin GaAs single-junction solar cells for self-powered skin-compatible electrocardiogram sensors. *Small Methods* **8**, 2301735 (2024).
29. Lee Sanchez, W. A., Sinha, S., Wang, P.-Y. & Horng, R.-H. Study on the performance of thin-film VCSELs on composite metal substrate. *Front. Optoelectron.* **16**, 32 (2023).
30. Zhang, Yu. Self-heating control of edge emitting and vertical cavity surface emitting lasers. *Elect.Theses Dissert.* 1324 (2014).
31. Qi, Y., Li, W., Liu, S. & Ma, X. Comprehensive design and simulation of a composite reflector for mode control and thermal management of a high-power VCSEL. *J. Opt. Soc. Am. B* **37**, 3487 (2020).
32. Huang, M. C. Y., Zhou, Y. & Chang-Hasnain, C. J. A surface-emitting laser incorporating a high-index-contrast subwavelength grating. *Nat. Photon.* **1**, 119–122 (2007).
33. Haghighi, N., Moser, P. & Lott, J. A. Power, bandwidth, and efficiency of single VCSELs and small VCSEL arrays. *IEEE J. Sel. Top. Quantum Electron.* **25**, 1–15 (2019).
34. Al-Omari, A. N. & Lear, K. L. Fabrication and performance of bottom-emitting flip-chip bonded 980 nm vertical-cavity lasers with copper- and indium-plated heat-sinks. *Semicond. Sci. Technol.* **26**, 125020 (2011).
35. Zhang, X. et al. A thermal analysis of stable-polarization VCSELs. *Optik* **157**, 203–207 (2018).
36. Lee, H. S. et al. Fiber-based quantum-dot pulse oximetry for wearable health monitoring with high wavelength selectivity and photoplethysmogram sensitivity. *npj Flex. Electron* **7**, 15 (2023).
37. Jang, I. et al. Improved optical efficiency of GaAs-based infrared vertical-cavity surface-emitting laser enabled by combining a metallic reflector and a Bragg reflector. *J. Vac. Sci. Technol.* **A41**, 063415 (2023).
38. Pan, P.-C. et al. Effect of thermal management on the performance of VCSELs. *IEEE Trans. Electron Devices* **67**, 3736–3739 (2020).
39. Persson, L. et al. Athermalization of the lasing wavelength in vertical-cavity surface-emitting. *Lasers Laser Photonics Rev.* **17**, 2300009 (2023).
40. Guan, Q., Laven, J., Bouten, P. C. P. & De With, G. Mechanical failure of brittle thin films on polymers during bending by two-point rotation. *Thin Solid Films* **611**, 107–116 (2016).
41. Yokota, T. et al. Ultraflexible organic photonic skin. *Sci. Adv.* **2**, e1501856 (2016).
42. Eun, H. J. et al. Strain-durable dark current in near-infrared organic photodetectors for skin-conformal photoplethysmographic sensors. *iScience* **25**, 104194 (2022).
43. Reddy, J. W., Lassiter, M. & Chamanzar, M. Parylene photonics: a flexible, broadband optical waveguide platform with integrated micromirrors for biointerfaces. *Microsyst. Nanoeng.* **6**, 85 (2020).
44. Yao, H. et al. Design, synthesis, and photovoltaic characterization of a small molecular acceptor with an ultra-narrow band gap. *Angew. Chem. Int. Ed.* **56**, 3045–3049 (2017).
45. Lee, G. H. et al. Stretchable PPG sensor with light polarization for physical activity–permissible monitoring. *Sci. Adv.* **8**, eabm3622 (2022).

Acknowledgements

This work was supported by the National Research Foundation (NRF) grant funded by Korean government (Ministry of Science and ICT) (Grant No. IITP-2023-2020-0-01461, RS-2023-00213089, RS-2024-00403639, RS-2025-25413074, RS-2024-00403163, and RS-2024-00437064). This work was supported by the NRF grant funded by the Korean government (Ministry of Education) (Grant No. RS-2021-NR060141). This work was supported by the NRF grant funded by the Korean government (Ministry of Trade, Industry & Energy) (Grant No. RS-2022-00154781). Following are results of a study on the "Gyeonggi Regional Innovation System & Education Project (Gyeonggi RISE Project)", supported by the Ministry of Education and Gyeonggi Province.

Author contributions

Y.Y. and J.J. contributed equally. Y.Y. fabricated VCSELs and performed electrical data analysis, and took the lead in drafting and writing the manuscript. J.J. fabricated ultraflexible OPD, integrated into the skin-conformal PPG sensors, and wrote the original manuscript. S.M., M.S., H.R., and S.K. supported data analyses. S.L. performed simulative analyses. J.-G.C. made significant contributions to revising and refining the manuscript. S.P. and J.L. conceived the research concept, secured funding, and supervised the project, providing guidance throughout its development and ensuring its successful completion. All authors contributed to the discussion on the manuscript.

Competing interests

The authors declare no competing interests.

Additional information

Supplementary information The online version contains supplementary material available at https://doi.org/10.1038/s41528-026-00572-2.

Correspondence and requests for materials should be addressed to Jun-Gyu Choi, Sungjun Park or Jaejin Lee.